

Driving Mechanism of Toroidal Rotation and Momentum Transport in JT-60U

M. Yoshida, Y. Koide, H. Takenaga, H. Urano, N. Oyama, K. Kamiya, Y. Sakamoto,
Y. Kamada and the JT-60 Team

Japan Atomic Energy Agency, Naka, Ibaraki-ken, 311-0193 Japan

e-mail contact of main author : yoshida.maiko@jaea.go.jp

Abstract. The driving mechanism of toroidal rotation and the momentum transport are studied, utilizing near-perpendicular neutral beam injection (PERP-NBI), co tangential and counter tangential NBI in JT-60U. Main results are as follows: (i) fast ion losses due to the toroidal field ripple induce the toroidal rotation in the direction antiparallel to the plasma current, i.e. counter (CTR) direction in the peripheral region, (ii) the magnitude of CTR rotation increases with increasing the ripple loss power in the peripheral region. (iii) Diffusive and non-diffusive terms of momentum transport are evaluated from the transient analysis by using the momentum source modulation experiment. Fast ion losses which locally induce the edge CTR rotation have been used as a novel momentum source. (iv) Parameter dependence of these transport coefficients i.e. the toroidal momentum diffusivity χ_ϕ and the convection velocity V_{conv} , and the relation between heat and momentum diffusivities are investigated in L and H-mode plasmas systematically. The toroidal momentum diffusivity increases with increasing heating power, and decreases with increasing the plasma current in L-mode plasmas. The H-mode exhibits momentum diffusivity better than L-mode. (v) We have also found that toroidal rotation velocity profiles in L-mode plasmas can be almost explained by momentum transport considering diffusivity and convective velocity estimated from the transient momentum transport analysis.

1. Introduction

It is now widely recognized that the burning plasmas in ITER and fusion reactors are highly self-regulating governed by strong linkages among pressure, current and rotation profiles [1]. In addition, recent tokamak researches have been emphasizing that the plasma rotation profile plays essential roles in determining confinement [2-4] and stability [5, 6]. In order to understand and operate this self-regulating system and to control the plasma rotation profile, we have to construct the physics basis on driving mechanism of rotation and on momentum transport, and those effects on plasma rotation profiles. There are several driving mechanisms of plasma rotation, such as external momentum source [3], fast ion losses [7], electron losses [8], and pressure gradient through the change of the radial electric field (E_r). The plasma rotation velocity and the radial electric field in the toroidal plasma are governed by the ion momentum balance equation as,

$$E_r = \nabla p_i / Z_i e n_i - V_p B_t + V_t B_p, \quad (1)$$

where p_i is the ion pressure, Z_i is the charge of the ion, e is the electronic charge, n_i is the ion density, V_p and V_t are, respectively, the poloidal and toroidal rotation velocities, and B_t and B_p are, respectively, the toroidal and poloidal magnetic fields.

In this report, we investigate two topics, one is the effect of the ripple loss of fast ions [9] on the toroidal rotation [7], and another is the momentum transport which influences the toroidal rotation profiles. In JT-60U, near-perpendicular neutral beam (PERP-NB) heated plasmas exhibit a toroidal rotation in the direction antiparallel to the plasma current, i.e. the counter (CTR) direction [10]. The injection angle of PERP-NBs is 75 degree with respect to the magnetic axis. An inward electric field induced by a ripple loss of fast ions was considered as

a candidate for the CTR rotation in the peripheral region [7, 10, 11]. We focus on the ripple-induced ion losses [9] as one of the driving mechanisms of plasma rotation. In order to reduce the toroidal field ripple, ferritic steel tiles (FSTs) have been installed inside the JT-60U vacuum vessel on the low field side [12].

Concerning momentum transport studies, only the diffusive terms of momentum transport has been discussed in most transport analysis [13], and experiments comparing L-mode and H-mode local transport rates have shown reduction in the, χ_ϕ , the ion thermal diffusivity (χ_i) and electron thermal diffusivity [13]. For the development of momentum transport studies, non-diffusive terms in the toroidal-momentum-transport equation are evaluated by the analysis of the transport of toroidal rotation in the transient phase with tangential NBs [14, 15]. However, the systematic dependence of these transport coefficients on plasma parameters and effects of these transport coefficients on the plasma rotation profiles have not been resolved. We have systematically investigated momentum transport coefficients in L and H-mode plasmas by using the driving source of CTR rotation. In this paper, the L-mode, where the spontaneous rotation induced by pressure gradient is much smaller than that by ripple losses, is chosen in order to investigate the basic mechanism of momentum transport. The operation regimes in L-mode plasmas are $\beta_N \sim 0.26-1$, $\rho^* \sim 0.04-0.05$ and $v^* \sim 0.04-0.26$, where β_N , ρ^* and v^* are normalized plasma pressure, normalized toroidal Lamore radius, and normalized collisionality. Moreover the H-mode ($\beta_N \sim 0.9$, $\rho^* \sim 0.05$ and $v^* \sim 0.04$) is chosen as the comparison with L-mode, in this study. We have separated diffusive and non-diffusive (convective) terms of momentum transport coefficients, and parameter dependence, such as plasma current, power, and density has been described. Moreover the relation between heat and momentum transport has been also investigated. We have found the effects of momentum transport on toroidal rotation velocity profiles in the core region.

2. Driving Mechanism of CTR Rotation with Perpendicular NBI

The CO or CTR toroidal rotation has been substantially observed with no external momentum input in such as perpendicular NBs [10], ICRF [7, 16], ECRF [8] heated plasmas on several devices. The candidates for driving sources of plasma rotation are considered ion and electron losses, pressure gradient. In this paper, we focus on the ripple-induced ion losses in several driving mechanisms of plasma rotation by using data with and without FSTs. The driving mechanism of CTR rotation and the location of the rotation driving source with PERP-NB injections are investigated using orbit following Monte Carlo (OFMC) code [17] and a beam perturbation experiment. In this paper, negative sign of V_t designates CTR directed rotation and positive sign of V_t CO directed rotation. The ripple amplitude defined as $(B_{\max} - B_{\min})/(B_{\max} + B_{\min})$, is varied by changing the plasma configuration. In this Section, experiments are carried out with large plasma volume $\text{Vol.} \sim 72-77 \text{ m}^3$ and middle plasma volume $\text{Vol.} \sim 65 \text{ m}^3$. For the plasma of $\text{Vol.} \sim 72-77 \text{ m}^3$, the maximum ripple amplitude was about 2% before installing FSTs, and for the plasma of $\text{Vol.} \sim 65 \text{ m}^3$, that was about 1%. The ripple amplitude reduces by $\sim 1/2$ due to FSTs. The ripple loss of fast ions is defined as the loss of energetic ions due to local mirror trapping (ripple trapped loss) and due to the lack of the up-down symmetry of banana orbit (banana diffusion). The ripple loss power is calculated by OFMC code.

2. 1. Relation between Ripple Losses and CTR Rotation

In JT-60U, the toroidal rotation velocity varies with the reduction of the toroidal field ripple by installing FSTs. This allows us to study the relation between ripple losses and CTR

rotation under a wide range in toroidal magnetic field ripple with other experimental conditions being similar by using data with and without FSTs. In Figs. 1(a)-(c), profiles of V_t , the ion temperature (T_i) and the electron density (n_e) in L-mode plasmas are shown, where solid circles show the data in the case with FSTs and open squares are the data in the case without FSTs. Main plasma parameters for these L-mode discharges are plasma current $I_p=1.15$ MA, $B_T=2.6$ T, the safety factor at 95% flux surface $q_{95}\sim 4.1$, and $\text{Vol.}\sim 65 \text{ m}^3$. The toroidal rotation is shifted to the CO direction by inserting FSTs. In these plasmas, only PERP-NBs are injected (the absorbed power $P_{\text{ABS}}\sim 1.4-1.8$ MW). Therefore, pressure gradients described in the first term on right-hand side of equation (1), in the case with and without FSTs are similar.

From these data, the difference in CTR rotation between the two discharges is not due to an increase in pressure gradient, which can enhance the inward electric field. The relation between V_t in the peripheral region $r/a\sim 0.9$, where a is the plasma minor radius, and the ripple loss power is investigated by NB power and the toroidal field ripple (with and without FSTs) scans, as shown in Fig. 1(d). In this data set, I_p , B_T , Vol. and the line averaged electron density (\bar{n}_e) are kept almost constant ($I_p=1.15$ MA, $B_T=2.6$ T, $q_{95}\sim 4.1$, $\text{Vol.}\sim 65 \text{ m}^3$, $\bar{n}_e\sim 1.5-2\times 10^{19} \text{ m}^{-3}$). Each arrow indicates the change in V_t by installing FSTs under the condition of almost same absorbed power (solid arrow: $P_{\text{ABS}}\sim 1.4-1.8$ MW, dotted arrow: $P_{\text{ABS}}\sim 2.8-3$ MW). As shown in Fig. 1(d), it is recognized that the systematic dependence of CTR rotation on the ripple loss of fast ions can be obtained by using data with and without FSTs. Figure 1(e) shows the individual contributions to E_r from the impurity pressure gradient and V_t terms on the right-hand side of equation (1) (i.e. $\nabla p_i/Z_i e n_i$ and $V_t B_p$) as a function of the ripple loss power. Here, the poloidal magnetic field at $r/a\sim 0.9$ is evaluated with the equilibrium reconstruction. The data set in Fig. 1(e) corresponds to that in Fig. 1(d). As shown in Fig. 1(e), the change in $V_t B_p$ with the ripple loss power is much larger than that in $\nabla p_i/Z_i e n_i$. The magnitude of V_p from the neoclassical theory is about 10 times smaller than that of V_t and the $-V_p B_t$ is comparable with $V_t B_p$. From these data, ion pressure gradient is not important for the trend of the increase in CTR rotation. The magnitude of CTR rotation reduces with FSTs as a consequence of the reduction in the ripple loss of fast ions, which can induce the inward electric field.

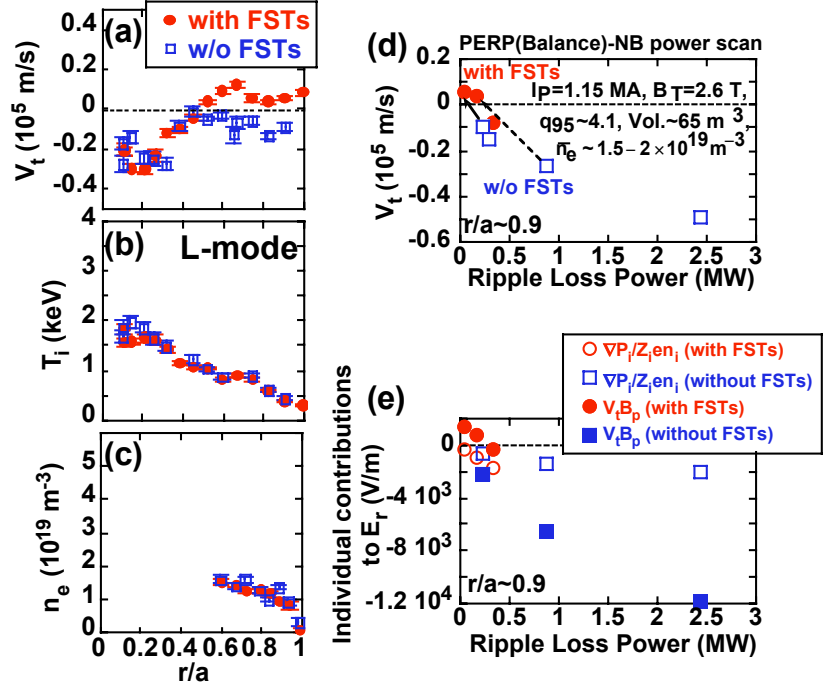


Fig. 1 Profiles of (a) V_t , (b) T_i and (c) n_e with and without FSTs in L-mode plasmas. The absorbed power $P_{\text{ABS}}\sim 1.4-1.8$ MW is almost same for both plasma discharges. (d) V_t dependence on the ripple loss power in the peripheral region with NB power and the toroidal field ripple scans. (e) The individual contributions to E_r from $\nabla p_i/Z_i e n_i$ and $V_t B_p$ on the right-hand side of equation (1) as a function of the ripple loss power. In these data set, $I_p=1.15$ MA, $B_T=2.6$ T, $q_{95}\sim 4.1$, $\text{Vol.}\sim 65 \text{ m}^3$ and the line averaged electron density (\bar{n}_e) are kept almost constant.

2. 2. Driving Source of CTR Rotation

In this section, the location of the driving source of CTR rotation is investigated in an L-mode plasma with large volume ($\text{Vol.} \sim 72 \text{ m}^3$) as shown in Fig. 2(a). The steady V_t profile in the L-mode plasma with FSTs is shown in Fig. 2(b). In this experiment, the plasma with low I_p ($I_p \sim 0.87 \text{ MA}$, $q_{95} \sim 8.2$) and large volume was selected in order to enhance ripple losses, therefore, CTR rotation is produced. In order to investigate the driving source due to the ripple loss of fast ions, we have evaluated the radial profile of the ripple loss of fast ions by the use of OFMC code. Figure 2(c) shows the time traces of ripple losses and charge exchange (CX) losses in Fig. 2(b) (input power $P_{\text{IN}} \sim 3.9 \text{ MW}$). The radial profiles of fast ions at birth and after the prompt loss (arrows in Fig. 2(c)) are shown in Fig. 2(d). The time-scale of ripple losses is much faster than slowing down time ($\tau_s \sim 0.4 \text{ s}$) and in such early time ($\sim 4 \text{ ms}$) CX losses is much smaller than the ripple losses, therefore, the hatched region ($0.7 < r/a < 0.9$) indicates the region where ripple losses mainly take place.

In order to confirm the location of the driving source of CTR rotation, beam perturbation techniques [10] are applied in the L-mode plasma. The beam line of the modulated beams is shown by the arrow in Fig. 3(a). In order that the central region is free from direct external momentum input, off-axis PERP-NBs ($P_{\text{IN}} \sim 3.9 \text{ MW}$) are injected with a square wave modulation at 2 Hz into a discharge similar to one shown in Fig. 2(b). Figure 3(b) shows the waveforms of

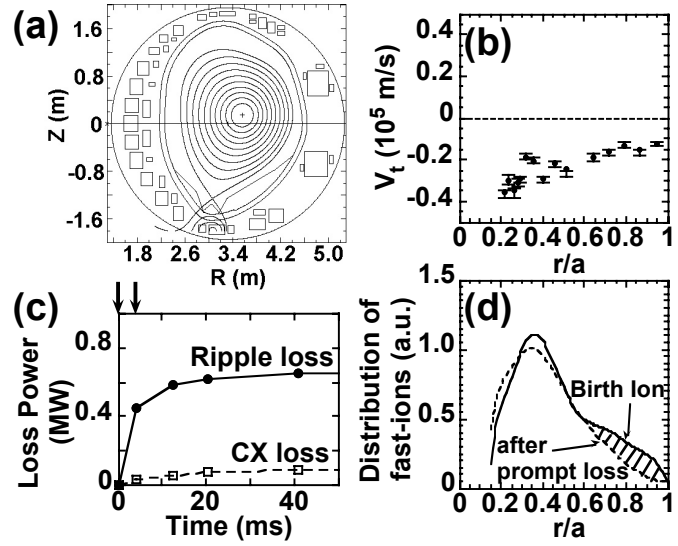


Fig. 2 (a) Plasma configuration with large volume. (b) Profile of the steady V_t with off-axis PERP-NB injections. (c) The time trace of lost power: the ripple loss power and the charge exchange (CX) loss power calculated using the OFMC code. (d) Profiles of fast ion at birth and after the prompt loss. The hatched region indicates the region where ripple losses mainly take place.

the response of V_t to modulated beams. Two traces of V_t at $r/a \sim 0.87$ and 0.23 are shown. Each trace is fitted to a sinusoidal function with the modulation frequency (dotted lines). Profiles of (c) modulated amplitude (V_{t0}), the prompt fast ion loss, (d) phase delay (ϕ) from PERP-NB perturbation techniques.

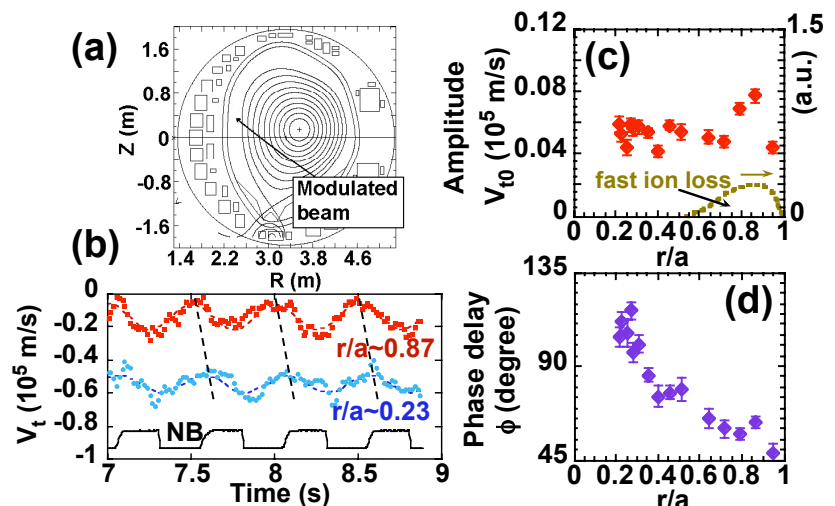


Fig. 3 (a) Plasma configuration with injection direction of modulated beams. (b) Response of V_t to modulated beams. Two traces of V_t at $r/a \sim 0.87$ and 0.23 are shown. Each trace is fitted to a sinusoidal function with the modulation frequency (dotted lines). Profiles of (c) modulated amplitude (V_{t0}), the prompt fast ion loss, (d) phase delay (ϕ) from PERP-NB perturbation techniques.

modulated V_t at $r/a \sim 0.87$ and 0.23 (solid lines). Each trace is fitted to a sinusoidal function at the modulation frequency (dotted lines). The radial profiles of the amplitude of the modulated part of V_t (V_{t0}) and of the phase delay of V_{t0} (ϕ) are shown in Figs. 3(c) and 3(d), respectively. The phase delay is taken from the start of NB injection. The prompt fast ion loss profile calculated by OFMC code is also shown in Fig. 3(c). Large amplitude and small ϕ are recognized in the peripheral region ($0.7 < r/a < 0.9$), and this region agrees with the location at which fast ion losses take place. This modulation brought about disturbances in \bar{n}_e and T_i in the region $0.2 < r/a < 0.7$ less than $\pm 5\%$ and $\pm 6\%$, respectively. Moreover, the phase delay of the modulated part of T_i is not observed such that of V_{t0} . These results indicate that fast ion losses due to the toroidal field ripple induce CTR rotation in the peripheral region.

3. Toroidal momentum transport

As shown in Fig. 2(b), CTR rotation is observed not only in the peripheral region but also in the core region. In order to clarify the driving mechanism of the core CTR rotation, V_t profiles in the core region are discussed from the viewpoint of moment transport [14] using V_{t0} and ϕ profiles shown in Figs. 3(c) and 3(d).

The momentum balance equations in the toroidal direction are written as

$$m_i n_i \frac{\partial V_t}{\partial t} = -\nabla \cdot M + S, \quad (2)$$

$$M = -m_i n_i \chi_\phi \frac{\partial V_t}{\partial r} + m_i n_i V_{conv} V_t, \quad (3)$$

where m_i , M , S , χ_ϕ and V_{conv} are the ion mass, the toroidal momentum flux, the toroidal momentum source, the toroidal momentum diffusivity and the convection velocity [14]. From equations (2) and (3), the time-independent solution of χ_ϕ and V_{conv} can be obtained [18]. In the region where the momentum source can be negligible, χ_ϕ and V_{conv} can be determined from the radial profiles of the amplitude and the phase of the modulated velocity (i.e. V_{t0} and ϕ profiles in Figs. 3(c) and 3(d)).

Figures 4(a) and 4(b) show χ_ϕ and V_{conv} as evaluated from above mentioned modulation analysis (i.e. V_{t0} and ϕ profiles in Figs. 3(c) and 3(d)) assuming the momentum source in the core region ($0.2 < r/a < 0.65$) to be negligible (M on the left-hand side of equation (3) is one orders of magnitude smaller than $-m_i n_i \chi_\phi \partial V_t / \partial r$ and $m_i n_i V_{conv} V_t$ at $r/a \sim 0.6$).

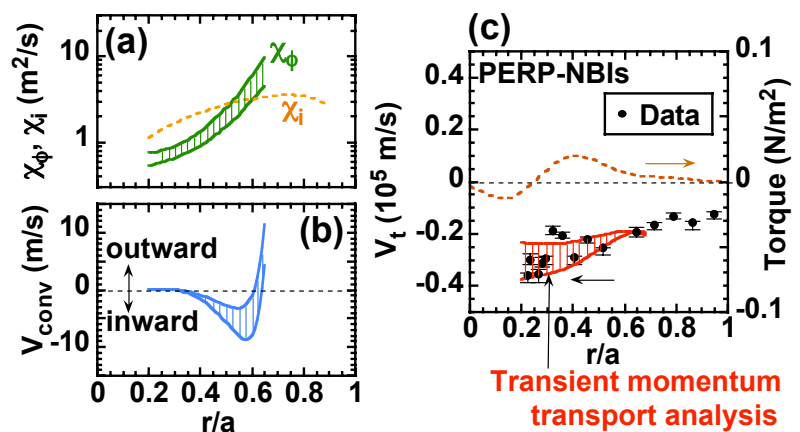


Fig. 4 Profiles of (a) the toroidal momentum diffusivity (χ_ϕ) and (b) the convection velocity (V_{conv}) obtained from beam perturbation techniques. (c) Experimental data (solid circles) in L-mode plasma with PERP-NBIs. Toroidal rotation velocity profile in the core region can be explained by momentum transport considering χ_ϕ and V_{conv} (solid lines). Torque profile (dashed line) is also shown.

These transport coefficients in the region $r/a > 0.7$ are not evaluated, because the driving source of CTR rotation is localized near the peripheral region as shown in Figs. 2 and 3. This momentum diffusivity is two or three orders of magnitude higher than the neoclassical value [19]. As is shown in Fig. 4(a), χ_ϕ is comparable to χ_i , and V_{conv} is about 5 m/s at $r/a \sim 0.5$ in this plasma. The first term on right-hand side of equation (3) is comparable to the second term on right-hand side of equation (3).

Next, we estimate V_t profile using the momentum transport coefficients χ_ϕ and V_{conv} . Experimental data (solid circles), which is the same data in Fig. 2(b), is shown in Fig. 4(c) again. Toroidal momentum source (torque) density profile (dashed line) is also shown. The solid lines show V_t profiles calculated from equation (3) using transport coefficients in Figs. 4(a) and 4(b) with the boundary condition at $r/a \sim 0.65$. As is shown in Fig. 4(c), V_t profile in the core region can be reproduced by momentum transport considering χ_ϕ and V_{conv} with PERP-NBIs. Thus, the toroidal rotation in the core region is dominated by the momentum transport with the coefficients shown in Figs. 4(a) and 4(b) in this L-mode plasma.

3. Momentum transport

3. 1. Characteristics of momentum transport coefficients

Parameter dependences of the momentum transport coefficients (i.e. χ_ϕ and V_{conv}) evaluated above-mentioned method are shown in this section. Experiments have been carried out to investigate the momentum transport as the heating power is varied under otherwise similar conditions. The result shown in Fig. 5 suggests that the degradation of momentum confinement with increasing heating power is observed similar to thermal confinement. The absorbed power range varied over the range $2 \text{ MW} < P_{\text{ABS}} < 10 \text{ MW}$. Over the entire power range, L-mode phase was maintained due to the high power threshold at the high $B_T > 3.8 \text{ T}$. The operation regimes in L-mode plasmas are $\beta_N \sim 0.26-1$, $\rho^* \sim 0.04-0.05$ and $v^* \sim 0.04-0.08$. Other plasma parameters for this series of discharges were $I_p \sim 1.5 \text{ MA}$, $B_T \sim 3.8 \text{ T}$, $\delta \sim 0.3$, $q_{95} \sim 4.2$ and $V_{\text{tot}} \sim 74 \text{ m}^3$. The profiles of momentum transport coefficients during this power scan are shown in Figs. 5(a) and 5(b). The momentum diffusivity χ_ϕ increases systematically as the power is increased, and the shape of χ_ϕ is nearly identical. The dependences of χ_ϕ and V_{conv} at $r/a \sim 0.6$ on absorption power are shown in Fig. 5(c). The data in H-mode phase is also plotted in Fig. 5(c). The H-mode exhibits momentum diffusivity better than L-mode by factor

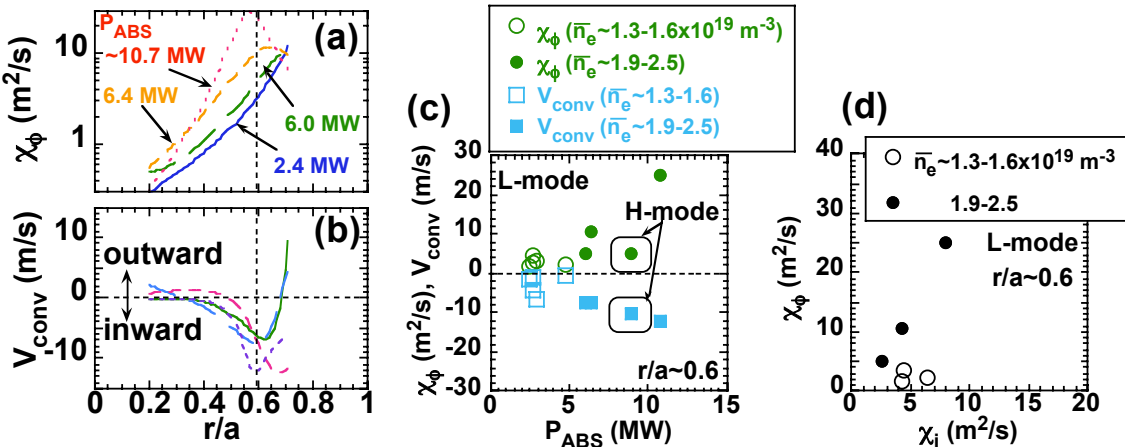


Fig. 5 Profiles of (a) χ_ϕ and (b) V_{conv} during a power scan in L-mode plasmas. (c) Dependence of χ_ϕ and V_{conv} at $r/a \sim 0.6$ on absorption power. (d) Relation between thermal χ_i and momentum diffusivities.

of 2-3. With the respect to comparisons of χ_ϕ and χ_i , although it was not the transient analysis, it was reported that χ_ϕ is similar to χ_i [13]. Comparisons of the momentum and thermal diffusivities at various values of power should therefore provide a strict test of whether the result in Fig. 4(a) is fundamental result. The comparison of χ_ϕ and χ_i during power scan is shown in Fig. 5(d). One can see that χ_ϕ increases with increasing χ_i . Experiments indicate a good correlation between the momentum transport and thermal transport.

We also investigate I_p dependence on χ_ϕ and V_{conv} . The thermal energy confinement for NB heated L-mode plasmas was found to scale linearly with the plasma current. The profiles of momentum transport coefficients during this I_p scan (0.87, 1.5, 1.77 MA) are shown in Figs. 6(a) and 6(b). For these plasma discharges, one CO tangential and one perpendicular NBs are injected with same power. Other plasma parameters for this series of discharges were $B_T \sim 3.8-4$ T, $\delta \sim 0.3$, $P_{\text{abs}} \sim 3.3-4$ MW, and $\bar{n}_e \sim 1.3-1.9 \times 10^{19} \text{ m}^{-3}$. The result shown in Fig. 6 suggests that the momentum confinement is increasing function of I_p . Figure 6(c) shows the steady $n_i V_t$ profile of these discharges, where n_i indicates the impurity density. The value of $n_i V_t$ increases with I_p at same torque input. This result is consistent with a decrease in χ_ϕ with increasing I_p . In this case, the pressure gradient (Fig. 6(d)), which can induce CTR rotation through the change of the radial electric field, is also larger at higher I_p . From these results, we can also suggest the momentum confinement increases in I_p .

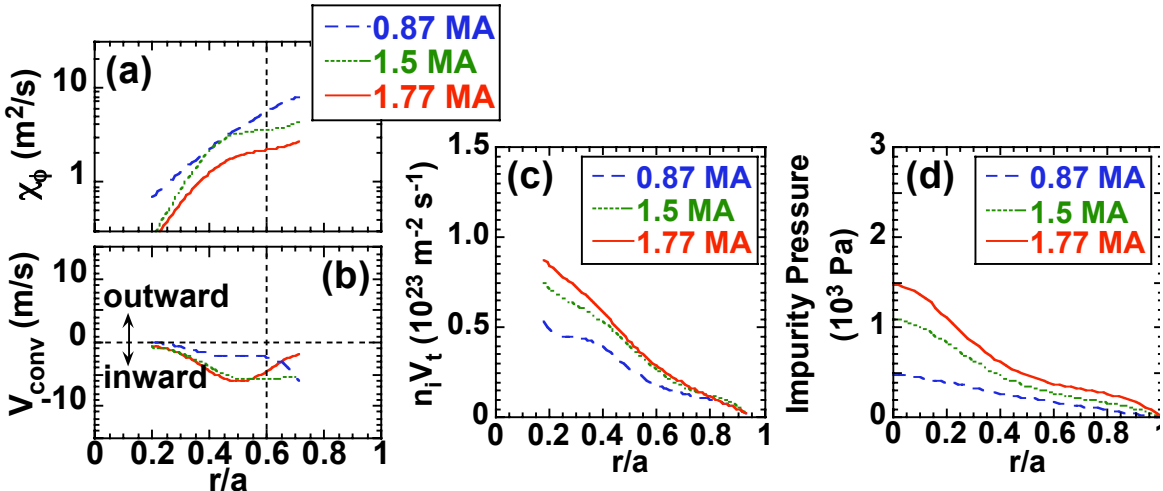


Fig. 6 Profiles of (a) χ_ϕ , (b) V_{conv} , (c) $n_i V_t$ (n_i : impurity density) and (d) impurity pressure gradient during a I_p scan in L-mode plasmas.

3. 2. Toroidal rotation velocity profile

In Fig. 4(c), we compare the measured V_t profile and calculation from equation (3) using transport coefficients with a PERP-NBs injected L-mode plasma. In this section, we treat the plasmas with momentum source, where CO and CTR tangential NBs are injected in order to

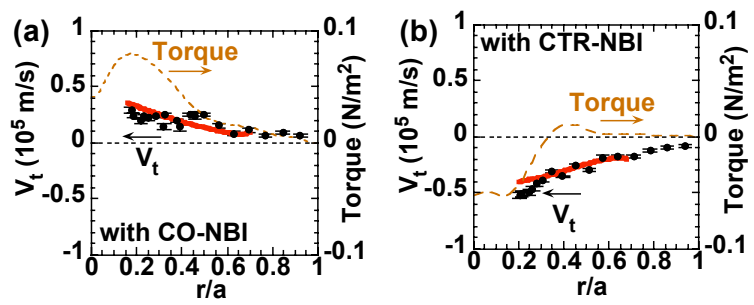


Fig. 7 Experimental data (solid circles) in L-mode plasmas (a) with CO-NBI, and (b) with CTR-NBI, respectively. Torque profiles (dashed lines) are also shown.

investigate whether the toroidal rotation in the core region is dominated by the momentum transport coefficients. The injection angle of tangential beams is 36 degree with respect to the magnetic axis. Experimental data (solid circles) in L-mode plasmas with CO-tangential NB ($I_p \sim 1.2$ MA $B_T \sim 3.8$ T, $\beta_N \sim 0.39$, $q_{95} \sim 5.7$ and $\bar{n}_e \sim 1.2 \times 10^{19}$ m⁻³) and CTR-tangential NB ($I_p \sim 0.87$ MA $B_T \sim 3.8$ T, $\beta_N \sim 0.34$, $q_{95} \sim 8.2$ and $\bar{n}_e \sim 1.6 \times 10^{19}$ m⁻³) are shown in Figs. 7(a) and 7(b), respectively. Torque profiles (dashed lines) are also shown. The solid lines show V_t profiles evaluated by the above-mentioned equation (3). The toroidal rotation profiles almost agree with calculations with CO and CTR-NBIs. The toroidal rotation profiles in the presence and absence of external torque have been explained by the momentum in the core region of L-mode.

4. Summary

In this report, we investigate the effects of the ripple loss of fast ions on the toroidal rotation by using data with and without FSTs. The magnitude of CTR rotation increases with increasing the ripple loss power in the peripheral region. Location of the driving source of CTR rotation agrees with the region where fast ion losses mainly take place. Besides V_t in the peripheral region, V_t profile in the core region is also discussed from the viewpoint of moment transport in an L-mode plasma. In the L and H-mode plasmas, χ_ϕ and V_{conv} are evaluated from transient momentum transport analysis. The transport coefficients χ_ϕ and V_{conv} increase systematically as the heating power is increased, and decrease with the plasma current. The toroidal rotation velocity profiles in the core region can be explained by momentum transport considering χ_ϕ and V_{conv} .

Acknowledgements

This work was partly supported by JSPS, Grant-in-Aid for Young Scientists (B) No 17740374. The authors acknowledge the members of the Japan Atomic Energy Agency who have contributed to the JT-60U projects.

References

- [1] Kamada Y 2000 *Plasma Phys. Control. Fusion* **42** A65
- [2] Ida K *et al* 1992 *Phys. Fluids* **B4** 2552
- [3] Sakamoto Y *et al* 2001 *Nucl. Fusion* **41** 865
- [4] Hahm T S and Burrel K H 1995 *Phys. Plasmas* **2** 1648
- [5] Ward D J *et al* 1995 *Phys. Plasmas* **2** 1570
- [6] Garofalo A M, Jensen T H and Strait E J 2002 *Phys. Plasmas* **9** 4573
- [7] Ida K *et al* 1991 *Nucl. Fusion* **31** 943
- [8] Idei H, Ida K *et al* 1994 *Phys. Plasma* **1** 3400
- [9] Connor J W and Hastie R J 1973 *Nucl. Fusion* **13** 221
- [10] Koide Y *et al* 1993 *Plasma Phys. Control. Nucl. Fusion Research* **1** 777
- [11] Romannikov A *et al* 2000 *Nucl. Fusion* **40** 319
- [12] Sakurai S *et al* "Reduction of toroidal magnetic field ripple with ferritic steel armors in JT-60U", submitted to *J. Nucl. Mater.*
- [13] ITER Physics Basis Expert Groups on Divertor and Divertor Modeling and Database, ITER Physics Basis Editors 1999 *Nucl. Fusion* **39** 2391
- [14] Nagashima K *et al* 1994 *Nucl. Fusion* **34** 449
- [15] Ida K *et al* 1998 *J. Phys. Soc. Jap.* **67** 4089
- [16] Eriksson L G *et al* 1992 *Plasma Phys. Control. Fusion* **34** 863
- [17] Shinohara K *et al* 2006 *J. Plasma and Fusion Research* **1** 007
- [18] Takenaga H *et al* 1998 *Plasma Phys. Control. Fusion* **40** 183
- [19] Hinton F L, Wong S K 1985 *Phys. Fluids* **28** 3082